# Enhanced Oxygen Evolution Reaction Performance Using Amorphous Hollow Cerium-Doped Cobalt Phosphate Derived from ZIF-67 Structures

Sina Maghool[a], Ali Akbar Asgharinezhad*[,b], Afsanehsadat Larimi*[,c], Cyrus Ghotbi[a], Farhad Khorasheh[a]

[a] Department of Chemical and Petroleum Engineering, Sharif University of Technology, Tehran, Iran

[b] Chemistry and Process Research Department, Niroo Research Institute, Tehran, Iran

[c] School of Engineering and Applied Sciences, Department of Chemical Engineering, Swansea University, Wales, UK

*Corresponding authors' Email: aasgharinezhad@nri.ac.ir (A. A. Asgharinezhad); a.larimi@swansea.ac.uk (A. Larimi)

**Abstract**

A major obstacle in achieving massive operations water splitting is the slow rate of the anodic reaction. To address this issue, metal phosphates have been extensively employed as efficient materials for the oxygen evolution reaction (OER). In this study, ZIF-67 structures were synthesized in both single-metal and bimetallic forms with different molar ratios of cerium. The structure with the best electrochemical activity ((5 present) cerium doped ZIF-67 ((5)CeZIF-67)) was subjected to a phosphatization process, resulting in the formation of the amorphous and hollow cerium doped cobalt phosphate (Ce-CPO) structure as a novel and highly efficient OER electrocatalyst. To the best of authors knowledge, this is the first report on the synthesis and application of Ce-CPO structure for boosting OER process. This resultant structure exhibited suitable electrochemical performance in the oxygen evolution reaction (OER), achieving an overpotential of 286 mV at a current density of 30 mA $cm^{-2}$ and a Tafel slope of 74.4 mV $decade^{-1}$. Furthermore, the final structure demonstrated satisfactory stability during a 10 h operation period. The notable improvement in the Ce-CPO structure was due to the use of a bimetallic framework combined with phosphorus and an amorphous porous structure. The distinctive configuration achieved greatly amplifies the effective surface area, hence improving electron transfer. The findings of this research can contribute to the development of electrodes with improved performance in OER.

**Keywords:** Metal phosphates, Oxygen evolution reaction, Amorphous and hollow structure, Cerium doped cobalt phosphate

## 1. Introduction

The growing need for energy, coupled with the swift depletion of conventional fossil fuels, has propelled the rapid advancement of efficient energy storage as well as conversion technologies [1,2]. Water splitting processes has prompted significant research because of its exceptional effectiveness in energy conversion and environmentally friendly characteristics [3,4]. This process is divided into two reactions: the cathodic hydrogen evolution reaction (HER), and the anodic oxygen evolution reaction (OER) [5,6]. The anodic process needs much more efficient materials because of its slow kinetics [7,8]. Ruthenium and iridium-based catalysts exhibit a comparatively small overpotential and demonstrate excellent catalytic activity in OER [9,10]. However, its expensive price and limited availability hinder its extensive utilization [11]. Given these factors, it is essential to make effective and strong electrocatalysts using materials that are plentiful on earth to study their efficacy in OER [12,13].

Recently, phosphate-based transition metals have shown significant promise as materials for electrochemical water splitting, owing to their proton-accepting capacity that enhances the oxidation of metal atoms and their tendency to alter catalyst structure [14]. For instance, Shaikh et al. [15] reported Ru-doped copper phosphate with an overpotential of 340 mV at a current density of 10 mA $cm^{-2}$. This work showed that using this phosphate-based structure creates an effective electrochemically active surface that improves ion transport at the electrode-electrolyte contact. Moreover, ZIF-67 is a structure with crystallinity and porosity that is created by combining organic ligands with cobalt ions [16]. It serves as an excellent intermediary for producing porous cobalt-based compounds, and there are several efficient techniques to enhance the performance of this structure in terms of OER optimization [17].

Firstly, the process of metal doping has the ability to enhance the catalytic performance [18]. Hence, bimetallic structures exhibit better adsorption and desorption behavior toward intermediates that have oxygen than monometallic materials [19]. Cerium (Ce) is an element that has a 4f electrons; metals with these kinds of electrons possess distinct chemical and electronic characteristics [20,21]. As a result, when 4f electrons are transferred, materials containing Ce often exhibit a smooth change from the +3 and +4 valence states [22,23]. This property allows for easy combination with 3d transition metals like cobalt (Co), which exists in the ZIF-67 structure, to control the distribution of electrons [24]. For example, Liu et al. [25] synthesized Ce-doped hollow mesoporous $NiCo_2O_4$ nanoprisms, which shows an overpotential of 290 mV at current density of 10 mA $cm^{-2}$. This research demonstrated that doping Ce into the MOF structure significantly enhances its performance in the OER.

Furthermore, surface structure engineering of a catalyst is an important approach for setting up its surface characteristics, which play a crucial role in defining the ultimate electrocatalytic activity in the OER [26]. In one hand, a hollow structure is advantageous for increasing both mass and electron transport, resulting in improved conductivity [27]. On the other hand, amorphous materials have attracted considerable interest because of their improved ability in OER [28,29]. Actually, amorphous structures provide a significant number of active sites, which greatly improves electrocatalytic activity [30]. Moreover, the presence of local structural disorder at short distances enhances the performance of the synthesized structure, as a result of the significant interaction between electrons and the lattice [31].

Given the mentioned factors and the synergistic effects they can have on improving the performance of electrocatalysts used in OER, in this study, the ZIF-67 structure was synthesized in both monometallic form and bimetallic form with cerium as a dopant. Furthermore, the effect

of the molar amount of cerium on the performance of this structure in the OER was investigated. After optimizing the cerium doping amount in the ZIF-67 structure, (5 present) cerium doped ZIF-67 ((5)CeZIF-67) (optimized material) underwent phosphatization process in a tube furnace, resulting in the formation of amorphous and hollow cerium doped cobalt phosphate (Ce-CPO) structure as a novel and highly efficient OER electrocatalyst. Additionally, to examine the beneficial effect of cerium incorporation in the final structure, we synthesized the CPO structure using the same method as for Ce-CPO. It was demonstrated that the bimetallic phosphatized Ce-CPO structure exhibited superior performance compared to the cobalt phosphate (CPO) structure. To the best of authors knowledge, this is the first report on the synthesis and application of Ce-CPO structure for boosting OER process. The synthesized materials underwent structural studies, including Fourier transform infrared spectrometer (FT-IR), X-ray diffraction (XRD), energy dispersive spectroscopy (EDS), inductively coupled plasma-optical emission spectrometry (ICP-OES), field emission scanning electron microscope (FESEM), and transmission electron microscope (TEM). Electrochemical analyses revealed that the optimization of the bimetallic structure of ZIF-67, followed by surface engineering on the optimized structure, led to improved electron transfer, increased active surface area, and consequently, the suitable performance of the Ce-CPO structure in the OER process. The Ce-CPO structure, when subjected to a current density of 30 mA $cm^{-1}$, had an overpotential of 283 mV. Furthermore, the Tafel slope recorded for this configuration was 74.4 mV $dec^{-1}$. Stability tests further confirmed that the Ce-CPO structure consistently maintained exceptional performance over extended usage, thereby showing its appropriateness for long-term applications.

## 2. Experimental

### 2.1. Materials

Cobalt(II) nitrate hexahydrate ($Co(NO_3)_2.6H_2O$), cerium(III) nitrate hexahydrate ($Ce(NO_3)_3.6H_2O$), sodium hypophosphite monohydrate ($NaH_2PO_2.H_2O$), 2-methylimidazole ($C_4H_6N_2$), potassium hydroxide (KOH), nitric acid ($HNO_3$), hydrochloric acid (HCl), acetone ($C_3H_6O$), *N*-methyl-2-pyrrolidone ($C_5H_9NO$), and carbon black (C) were purchased from Merck (Germany). Nickel foam (NF, thickness:0.3 mm) was obtained from American Elements (United States). Polyvinylidene fluoride ($-(C_2H_2F_2)_n-$) was purchased from Alfa Chemistry (United States). Methanol ($CH_3OH$) with purity of (99%) was obtained from Neutron Pharmacochemical Co (Iran).

### 2.2. Synthesize of ZIF-67, (X)CeZIF-67 (X=1, 3, 5, 7), CPO and Ce-CPO

In order to synthesize the ZIF-67 structure, a solution was prepared by dissolving 0.0039 mol of cobalt in 30 ml of methanol in beaker A. In beaker B, 0.0159 mole of 2-methylimidazole were dissolved by adding and mixing 30 ml of methanol. Subsequently, the solution contained in beaker B was gradually introduced into beaker A, resulting in the transformation of the solution into a purple color. The resulting combination was then agitated for a duration of 30 minutes. The resultant solution was allowed to remain undisturbed at ambient temperature for a duration of 24 h, after which the resulting precipitate was subjected to three successive washes using pure methanol. Afterwards, the sample was subjected to a drying process for a duration of 12 h at a temperature of 60 °C inside an oven in order to get ZIF-67.

To synthesize the bimetallic structure, 0.003861 mol of $Co(NO_3)_2.6H_2O$ and 0.000039 mol of $Ce(NO_3)_3.6H2O$, were dissolved in methanol. The previous procedure was then repeated. The powder obtained was designated as (1 present) cerium doped ZIF-67 ((1)CeZIF-67). Similarly, the synthesis was conducted using three, five, and seven molar percentage of cerium, resulting in the formation of (X)CeZIF-67 (X = 3, 5, 7), respectively.

For the synthesis of the Ce-CPO structure, 0.1 g of the optimized bimetallic structure ((5)CeZIF-67) was placed in one porcelain boat, and then 0.5 g of $NaH_2PO_2.H_2O$ was added to another porcelain boat. These boats were placed in a tube furnace under a nitrogen atmosphere for the phosphatization process. The process was carried out at 300 °C with a heating rate of 5 °C per min and maintained at this temperature for 2 h. The resulting material was named Ce-CPO. To better compare the electrochemical performance, CPO was synthesized using the monometallic ZIF-67 structure following the same method.

### 2.3. Materials characterization

The FT-IR spectra were obtained using the PerkinElmer instrument (United States), including a wavelength region of 4000−400 $cm^{-1}$. The X-ray diffraction (XRD) analyses of the materials have been recorded utilizing a PANalytical equipment (United Kingdom) with Cu−Kα radiation. The elemental mapping properties of synthesized materials were assessed utilizing energy dispersive spectroscopy (EDS) using the TESCAN (Czech Republic) instrument. The electron microscopy was used to analyze the morphology and structure of the produced samples (FE-SEM, TESCAN (Czech Republic); TEM, Zeiss (Germany)). The Ce content of the synthesized materials was determined using inductively coupled plasma-optical emission spectrometry (ICP-OES) on a Varian-Inc (United States) equipment.

### 2.4. Electrochemical measurements

The working electrode was fabricated by the following procedure. Initially, nickel foam, cut into 1 x 1 $cm^2$ pieces, was subjected to ultrasonic waves in acetone, 2 M KOH solution, and 1 M HCl solution for 10, 4, and 2 min, respectively. Finally, it was treated with ultrasonic waves in acetone for 5 min and then dried at room temperature. Subsequently, a solution of $C_5H_9NO$ and $(C_2H_2F_2)_n$

was prepared in a 9:1 weight ratio. A mixture containing 12 mg of the synthesized catalyst and 2 mg of carbon black was then dissolved in this solution. The resulting slurry was then applied to the surface of the NF. Ultimately, the NF that had been coated was subjected to a temperature of 120 °C in an oven for a duration of 2 h.

An electrochemical workstation (RADstat, Kianshar Danesh, Iran) was used to perform electrochemical evaluations of synthesized structures. The electrochemical evaluations were performed utilizing a three-electrode setup. Ag/AgCl (sat. KCl) and platinum (Pt) wire were used as reference and counter electrodes, respectively. The working electrodes were the coated NFs, which were mentioned previously. A 1.0 M solution of KOH was used as the electrolyte for electrochemical measurements. The potentials were determined with respect to a reversible hydrogen electrode (RHE), which is demonstrated by the equation (1).

$$E_{RHE} = E_{Ag/AgCl} + E^{0}_{Ag/AgCl} + 0.059\ pH \quad (1)$$

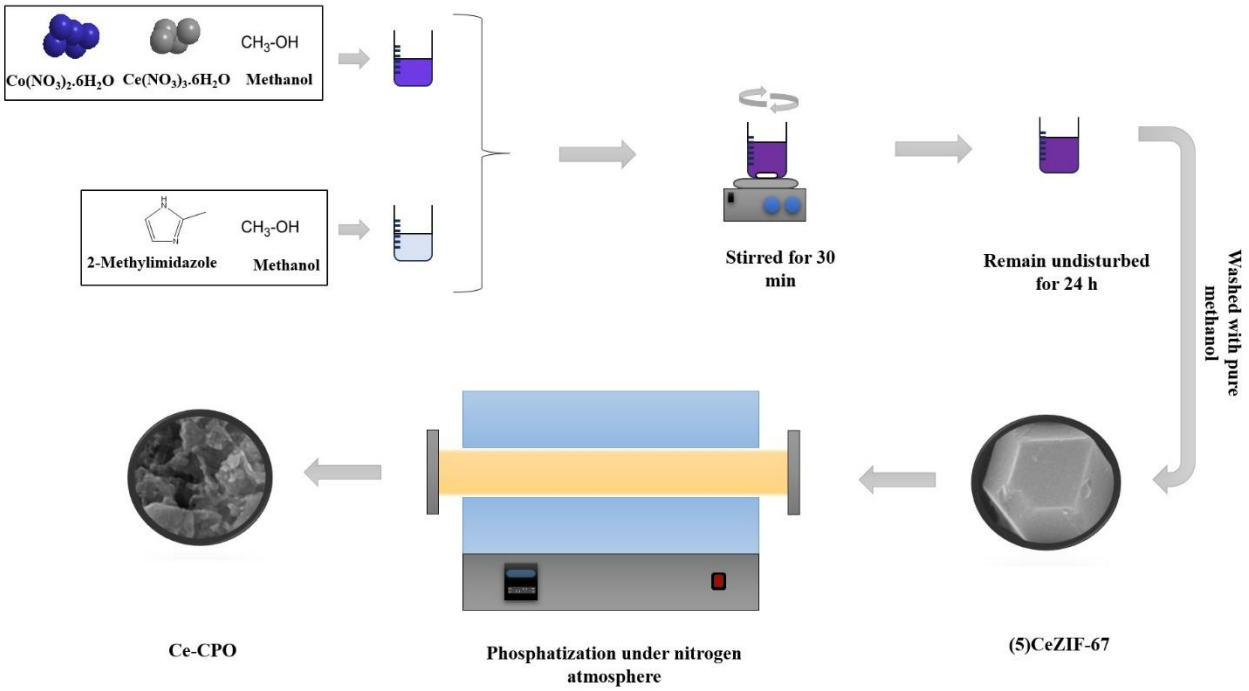

Scheme 1. Schematic of synthesis for Ce-CPO

## 3. Results and discussion

### 3.1. Materials characterization

The Ce-CPO were synthesized following the technique shown in Scheme 1. FT-IR analysis was performed to examine the functional groups of the synthesized materials, and the spectrum of all single-metal and bimetallic ZIF-67 structures is visible in Fig. 1a. The peak at 425 $cm^{-1}$ indicates the Co-N stretching mode [32]. The peaks in the range of 600 to 1500 $cm^{-1}$ represent the stretching and bending modes of the imidazole ring, alongside the peak at 1584 $cm^{-1}$ which is related to the C=N stretching bond [33–35]. Additionally, the peaks at 2925 and 3128 $cm^{-1}$ respectively represent the aliphatic and aromatic C-H bonds [36,37]. All these peaks in the single-metal and bimetallic structures with different ratios of Ce confirm that the materials are well-synthesized and consistent with the ZIF-67 structure.

Furthermore, as shown in Fig. 4a, the phosphatization of the (5)CeZIF-67 structure resulted in the disappearance of some previous peaks and the emergence of new peaks in the FT-IR spectrum of Ce-CPO. This indicates the effectiveness of the phosphatization process in altering the structure and forming new bonds. Specifically, the peaks at 1080 and 908 $cm^{-1}$ indicate the asymmetric and symmetric stretching of $PO_4^{3-}$, respectively [38]. Additionally, the peak that appears at 540 $cm^{-1}$ is related to the stretching mode of $PO_4^{3-}$ [39].

XRD analysis was performed on the manufactured substances in order to determine their crystalline structure. The peaks of ZIF-67 are illustrated in Fig. 1b at specific 2θ angles: 7.32, 10.70, 12.80, 14.79, 16.68, and 18.28. Additionally, the peaks also confirm the structural arrangement of ZIF-67 [40]. The planes associated with the specified angles could be observed in

Fig. 1b. The bimetallic structures exhibit diffraction peaks at identical angles with strong intensity, demonstrating their homogeneous synthesis and high crystallinity [41]. The incorporation of Ce with different ratios into the ZIF-67 structure has not caused any major alteration in its crystalline phase, thereby highlighting the dopant role of Ce in the ZIF-67 structure [42]. Moreover, the observed pattern for the Ce-CPO structure reveals the absence of distinguishable peaks, indicating its amorphous structure. Additionally, to better compare the structures, the rescaled XRD image in the 2θ range of 0 to 30 degrees is shown in Fig. 1c.

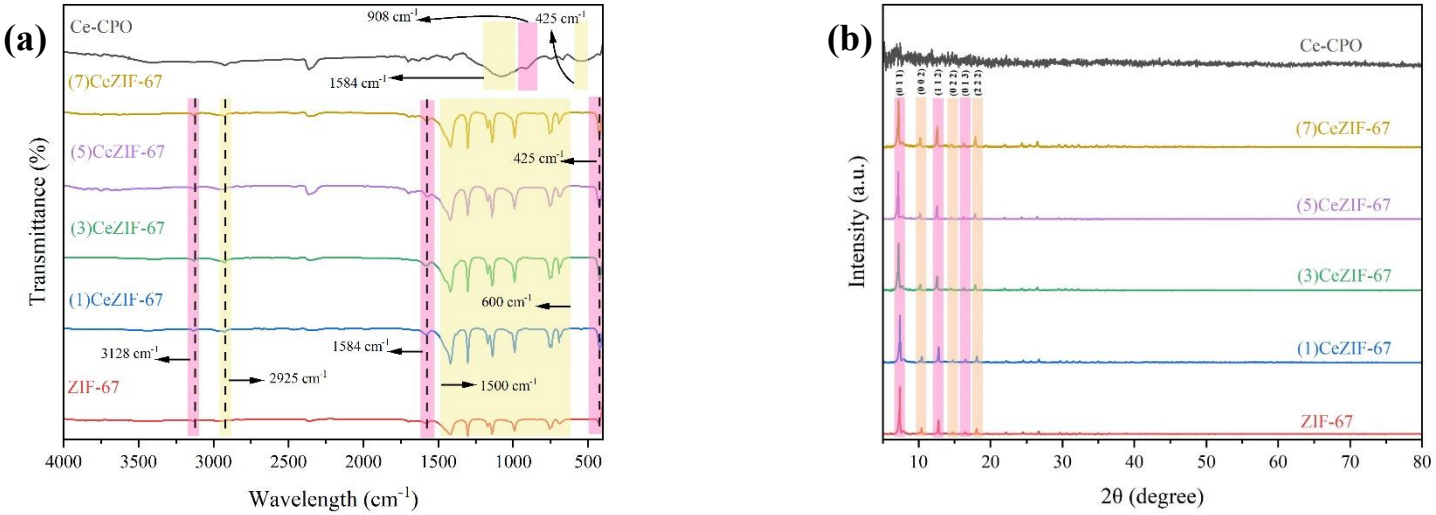

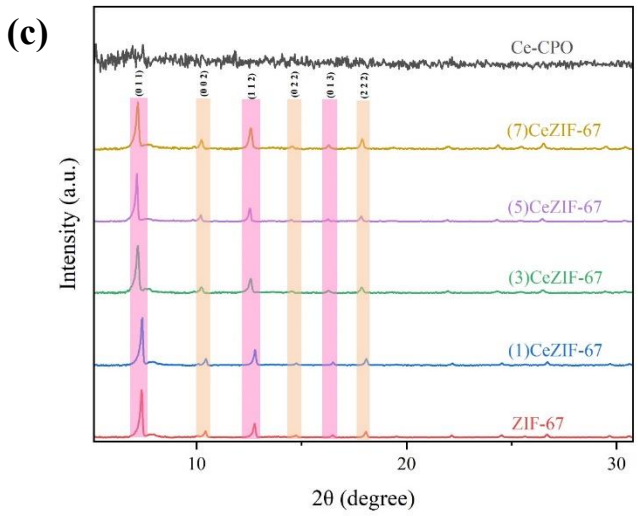


**Fig. 1.** (a) FT-IR spectra and (b) XRD patterns of ZIF-67, (1)CeZIF-67, (3)CeZIF-67, (5)CeZIF-67, (7)CeZIF-67, and Ce-CPO; (c) The XRD patterns of ZIF-67, (1)CeZIF-67, (3)CeZIF-67, (5)CeZIF-67, (7)CeZIF-67, and Ce-CPO were recorded in the 2θ range from 0 to 30 degrees.

EDS analysis was utilized to investigate the elemental dispersion and to examine the weight percentages of elements present on the surface of the synthesized materials. In Fig. (S1-S5, Electronic Supplementary File), EDS analyses and elemental mapping of the structures ZIF-67, (1)CeZIF-67, (3)CeZIF-67, (5)CeZIF-67, and (7)CeZIF-67 are respectively presented. The EDS spectrum indicates the presence of carbon (C), nitrogen (N), oxygen (O), and cobalt (Co) elements in the ZIF-67 structure. Furthermore, the structures (1)CeZIF-67, (3)CeZIF-67, (5)CeZIF-67, and (7)CeZIF-67 contain the cerium (Ce) element in addition to the elements present in the ZIF-67 structure. Additionally, the elemental mapping of these structures shows that all elements are uniformly dispersed across the surface, indicating the appropriate synthesis of the desired structures.

Moreover, Fig. (2a-2g) exhibit the EDS analysis and elemental mapping of the Ce-CPO structure. This research demonstrates that phosphorus has been assimilated into the structure as a result of the phosphatization process and the degradation of some organic ligands. The atomic ratio of cobalt to phosphorus (Co:P) in the Ce-CPO structure is around 3:1.73, which closely matches the predicted ratio of 3:2 [43]. This outcome validates the existence of the $Co_3(PO_4)_2$ structure [44]. Additionally, the elemental mapping indicates a uniform dispersion of elements such as carbon (C), cerium (Ce), cobalt (Co), nitrogen (N), oxygen (O), and phosphorus (P) throughout the structure. This demonstrates the effective integration and even distribution of these elements within the Ce-CPO structure.

To accurately assess the presence of Ce in the structures and ensure its incorporation, ICP-OES analysis was employed. Initially, the targeted structures were dissolved in 1.0 mL of acid, prepared by mixing HCl and $HNO_3$ in a 3:1 ratio, and then diluted to the desired volume. The ICP-OES analysis revealed that the cerium content in the (1)CeZIF-67, (3)CeZIF-67, (5)CeZIF-67, (7)CeZIF-67, and Ce-CPO structures was 0.47%, 0.72%, 1.44%, 1.54%, and 1.33% by weight, respectively. The results indicate that as the amount of cerium added during the synthesis increased, the cerium content incorporated into the bimetallic ZIF-67 structure also increased.

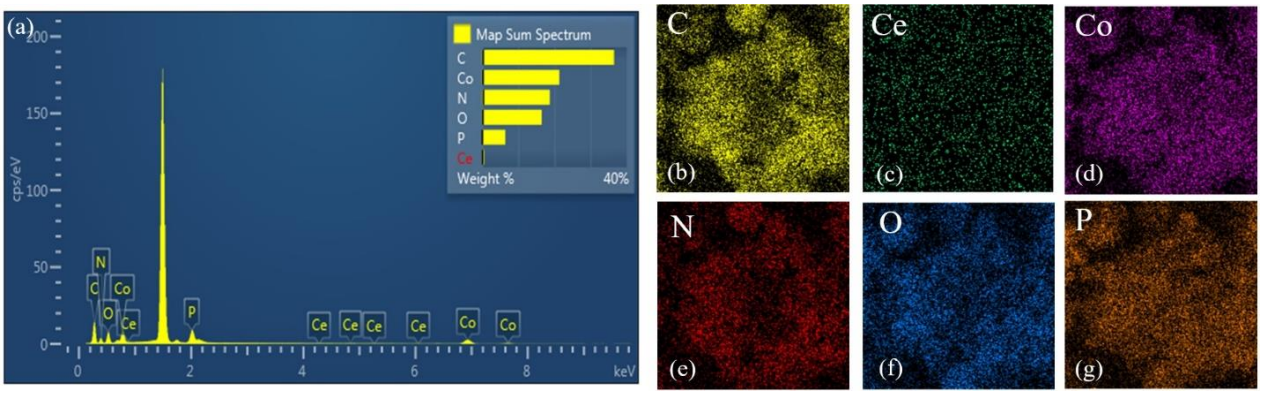


**Fig. 2.** (a) EDS spectrum of the Ce-CPO; (b-g) elemental mapping of Ce-CPO.

To examine the structure of the synthesized particles, FE-SEM images were utilized. Fig. 3a displays the ZIF-67 structure, which clearly shows that the ZIF-67 nanocrystals possess a rhombic dodecahedral formation. Fig. (3b – 3e) clearly demonstrate that the addition of cerium with various ratios to the ZIF-67 structure has not significantly affected the structure, and the polyhedral shape is well-preserved. Additionally, in Fig. 3f, the FE-SEM image of Ce-CPO is visible. The image clearly shows that through the phosphatization process, the (5)CeZIF-67 structure has transformed into a porous and hollow structure. Moreover, as observed in the FE-SEM micrographs of the CPO structure (Fig. S6a, Electronic Supplementary File), the phosphatization process, similar to that in the Ce-CPO structure, has resulted in the formation of a porous and hollow structure.

TEM analysis was utilized for further investigating the morphology of the CPO and Ce-CPO structure. The TEM micrographs in Fig. S6b (Electronic Supplementary File) and Fig. (3g, 3h) clearly depict a porous and hollow structure, which aligns with the findings from the FE-SEM investigation [45].

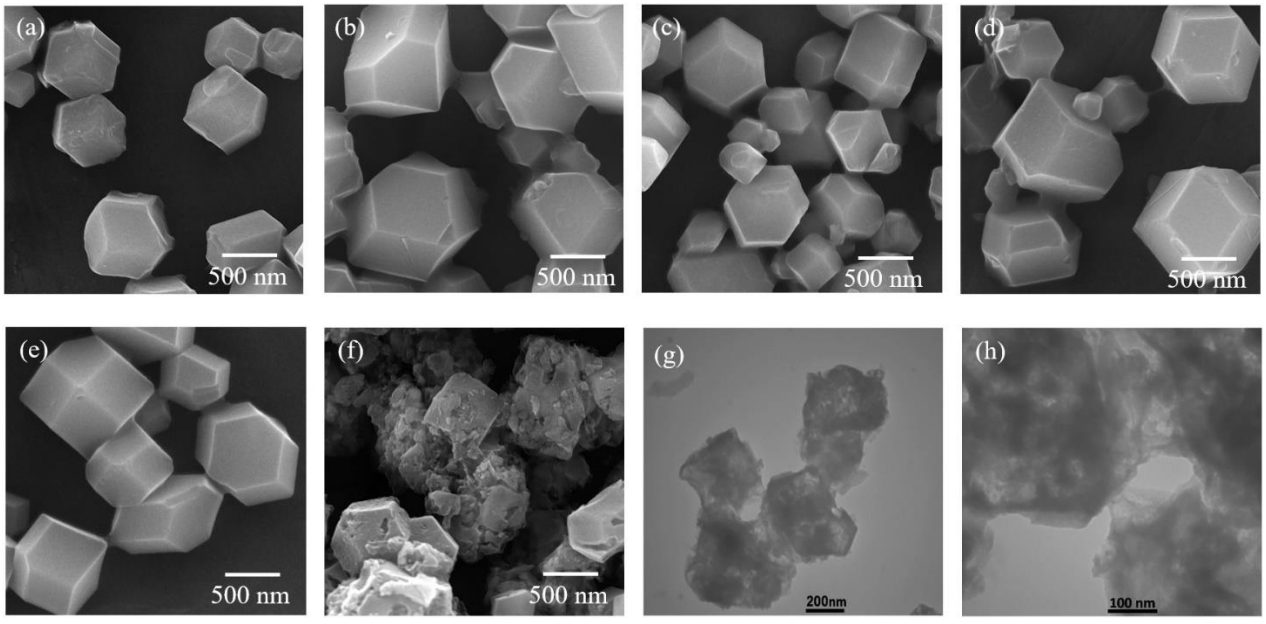

**Fig. 3.** FE-SEM micrographs of (a) ZIF-67, (b) (1)CeZIF-67, (c) (3)CeZIF-67, (d) (5)CeZIF-67, (e) (7)CeZIF-67, and (f) Ce-CPO; (g,h) TEM micrographs of Ce-CPO.

### 3.2. Electrochemical measurements

The electrocatalytic activity of the produced compounds for the OER was examined using linear sweep voltammetry (LSV) in a range of 1.0 to 1.7 V vs. RHE with a scan rate of 5 mV $s^{-1}$. As shown in Fig. 4a, the performance of the electrocatalysts ZIF-67, (1)CeZIF-67, (3)CeZIF-67, (5)CeZIF-67, (7)CeZIF-67, CPO, and Ce-CPO has been evaluated, displaying overpotentials of 411, 409, 393, 381, 396, 300, and 286 mV, respectively, at a current density of 30 mA $cm^{-2}$. The results indicate that the performance of the ZIF-67 structure improved due to bimetallic modification with Ce, mainly because of the increased active sites and consequently better electron transfer [46]. This performance is optimized in the (5)CeZIF-67 structure. The findings suggest that including an optimal quantity of cerium (Ce) into the ZIF-67 framework can augment its electrochemical efficacy. It has been reported that Ce sites play a significant role in the OER process by enhancing the adsorption of $O_2$ onto the catalyst surface. These sites facilitate the dissociation of adsorbed $O_2$ into O atoms, which are essential for the OER. Moreover, the Ce sites contribute to the formation of oxygen vacancies, which support the dissociation of water molecules, further enhancing the overall electrocatalytic performance [47]. In addition, cobalt (Co) plays a crucial function in enhancing the performance of the electrocatalyst in the process of OER. A larger concentration of Co improves the probability of CoOOH formation during OER, hence improving efficiency of the electrocatalyst [48]. The enhanced performance of the redesigned structure can be attributed to the presence of an ideal quantity of Ce and Co metals within the structure. Furthermore, as demonstrated, the electrocatalytic performance of both CPO and Ce-CPO structures showed a significant improvement after the phosphatization process compared to

their initial states. This indicates the positive effect of this process on enhancing the structure and performance of the electrocatalysts. Additionally, the Ce-CPO structure exhibited better performance compared to the CPO structure without the Ce metal, highlighting the improved performance due to the bimetallic nature of the final structure. Moreover, the enhancement can be credited to the formation of a porous structure, which increases the active surface area that is vital for improving the OER process [49].

The Tafel slope is a highly suitable parameter for examining the kinetics of electrochemical reactions. Based on the following equation, the Tafel slope was determined [50]:

$$\eta = b \log (j/j_0) \quad (2)$$

where b, j, $j_0$, and η refer to Tafel slope, current density, exchange current density, and overpotential, respectively. Fig. 4b illustrates the Tafel plots (determined using equation (2)) for the produced structures. The Tafel slopes found for ZIF-67, (1)CeZIF-67, (3)CeZIF-67, (5)CeZIF-67, (7)CeZIF-67, CPO, and Ce-CPO were 121.0, 114.1, 106.7, 102.0, 112.3, 81.5, and 74.4 mV $decade^{-1}$, respectively. The results obtained demonstrate the effectiveness of the strategies used to enhance the electrochemical performance of the catalysts for OER. The bimetallic modification of the initial structure followed by optimizing the amount of Ce in ZIF-67 significantly reduced the Tafel slope. This indicates that an appropriate amount of Co and Ce metals is present in the optimized structure, aiding the reaction kinetics to reach their peak in the bimetallic ZIF-67 structure. Ultimately, the Tafel slope for the Ce-CPO structure reached its lowest level, indicating the fastest OER reaction kinetics among the synthesized structures. Moreover, the higher Tafel slope observed for CPO compared to Ce-CPO indicates that, alongside the structural improvements achieved through the phosphatization process, the presence of an appropriate amount of cerium also plays a significant role in enhancing the reaction kinetics. The decreasing

trend in the Tafel slope indicates that the approach used in the synthesis of the materials has been suitable.

Fig. 5 displays the observed overpotentials at current densities of 30 and 40 mA $cm^{-2}$, as well as the Tafel slopes of the compounds.

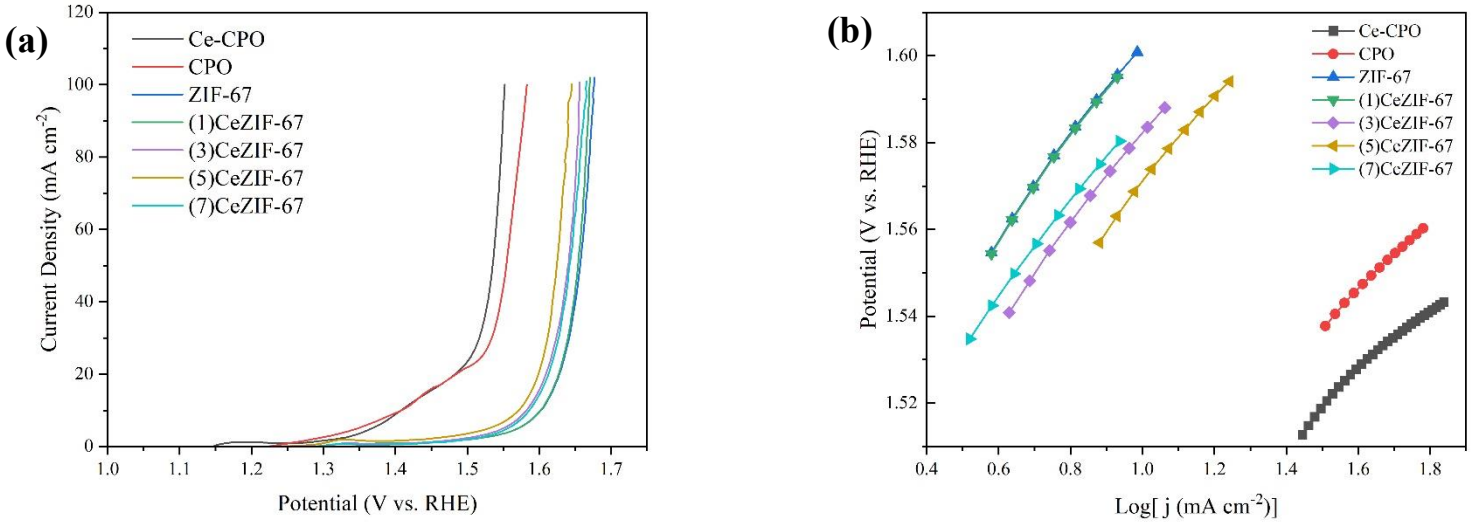


**Fig. 4.** (a) LSV curves and (b) Tafel plots of ZIF-67, (1)CeZIF-67, (3)CeZIF-67, (5)CeZIF-67, (7)CeZIF-67, CPO, and Ce-CPO.

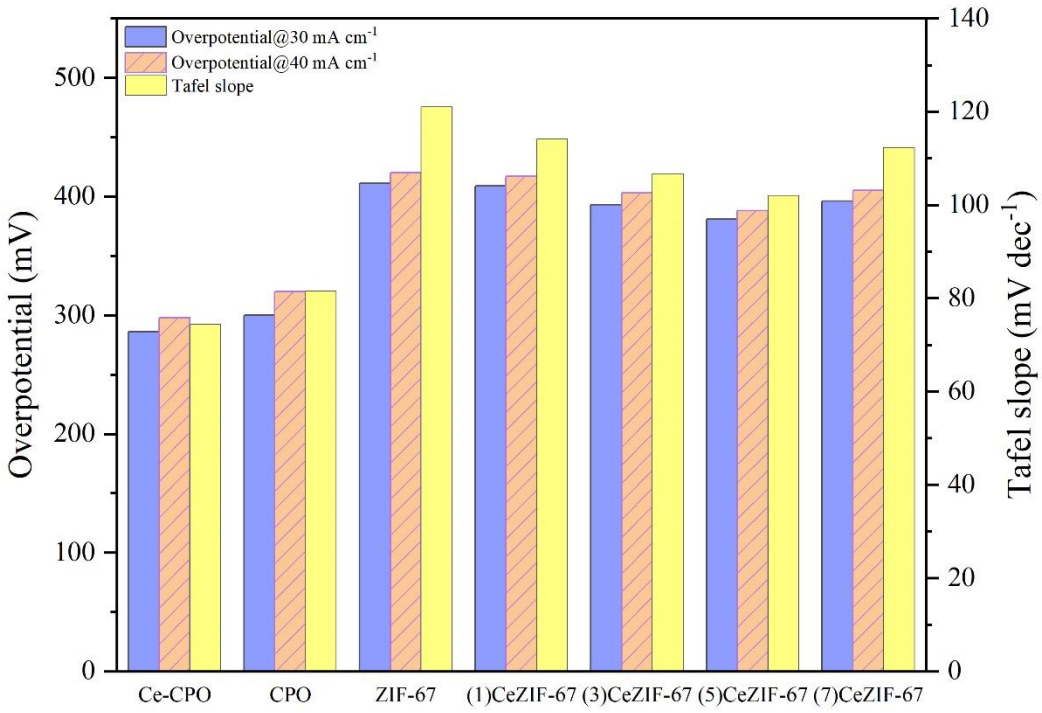


297

298 **Fig. 5.** Measured overpotentials in different current densities, and Tafel slopes of ZIF-67,
299 (1)CeZIF-67, (3)CeZIF-67, (5)CeZIF-67, (7)CeZIF-67, CPO, and Ce-CPO.

300 The method of electrochemical impedance spectroscopy (EIS) was utilized to gain a more
301 comprehensive understanding of the kinetics of OER, which was conducted within the frequency
302 range of 0.1–$10^5$ Hz. As shown in Fig. 6a, the Nyquist plots of the synthesized compounds are
303 displayed, and the obtained results have been fitted to an equivalent circuit model, which is
304 depicted in the diagram included in Fig. 6a. $R_s$ represents the solution resistance, whereas $R_{ct}$
305 indicates the charge transfer resistance linked to the OER occurring at the interface between the
306 catalyst and the solution. The $R_{ct}$ values for structures ZIF-67, (1)CeZIF-67, (3)CeZIF-67,
307 (5)CeZIF-67, (7)CeZIF-67, CPO, and Ce-CPO are respectively 24.99, 24.27, 20.44, 18.64, 22.16,

8.72, and 6.28 Ω. The results suggest that the introduction of Ce into the structure and the phosphating of the bimetallic structure led to an improvement in electron transfer in the amorphous hollow compound [51]. The Rs values employed to adjust for the ohmic drop caused by the solution are 4.59, 4.50, 4.11, 4.05, 4.35, 3.83, and 3.60 Ω for ZIF-67, (1)CeZIF-67, (3)CeZIF-67, (5)CeZIF-67, (7)CeZIF-67, CPO, and Ce-CPO , respectively.

The electrochemical active surface area (ECSA) level is a crucial parameter for evaluating the performance of electrocatalysts. To compute ECSA, the value of the double-layer capacitance ($C_{dl}$) needs to be determined first. This parameter was obtained using cyclic voltammetry (CV) testing, where scans were performed at various scan rates in the non-Faradaic region of the materials (Fig. S7, Electronic Supplementary File).

It is noteworthy that $C_{dl}$, which correlates directly with ECSA, is derived from plotting Δj at a constant voltage versus scan rate [52]. The results from Fig. 6b indicate that $C_{dl}$ values for ZIF-67, (1)CeZIF-67, (3)CeZIF-67, (5)CeZIF-67, (7)CeZIF-67, CPO, and Ce-CPO materials are 0.32, 0.35, 0.44, 0.53, 0.41, 1.12, and 1.49 mF $cm^{-2}$ respectively. These findings suggest that initially, (5)CeZIF-67 exhibited the highest $C_{dl}$ value, indicating successful optimization of cerium incorporation into the ZIF-67 structure.

Subsequently, the results for CPO and Ce-CPO indicate that the bimetallic composition of the final structure, incorporating an optimal amount of Ce, and the utilization of a suitable phosphatization method for ZIF-67 based structures yielded remarkable results, leading to a significant enhancement in the $C_{dl}$ value.

Since, according to equation (3), $C_{dl}$ is directly proportional to ECSA, where $C_s$ is a constant, ECSA values vary accordingly for the mentioned materials. Initially, ECSA reached an optimal

state for (5)CeZIF-67, and thereafter, due to phosphatization process, it achieved its best state. The improvement in ECSA signifies a greater number of active sites for the electrochemical process, leading to enhanced electron transfer rate [53].

$$ECSA = C_{dl}/C_s \quad (3)$$

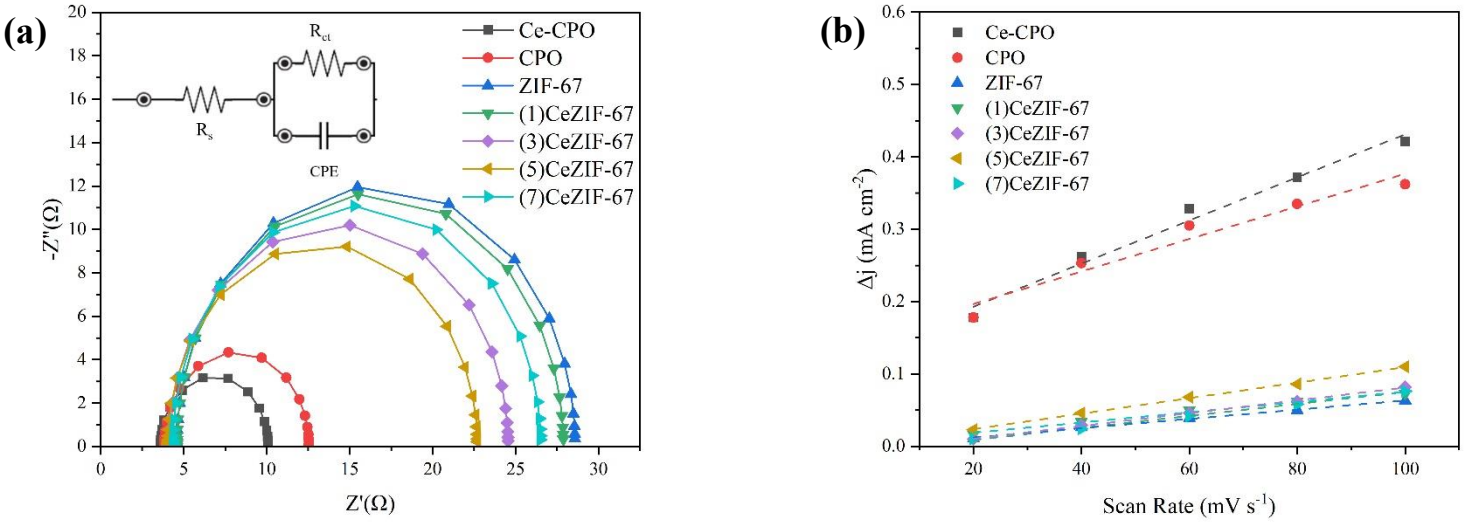


**Fig. 6.** (a) Nyquist diagrams of ZIF-67, (1)CeZIF-67, (3)CeZIF-67, (5)CeZIF-67, (7)CeZIF-67, CPO, and Ce-CPO (inside schematic represents an equivalent circuit); (b) The electrochemical double layer capacitance of ZIF-67, (1)CeZIF-67, (3)CeZIF-67, (5)CeZIF-67, (7)CeZIF-67, CPO, and Ce-CPO. (The solid lines depict the linear regression model that has been applied to the dataset.)

In addition to the OER operation, the long-term durability of electrodes is also an important factor in assessing their usage [54]. Consequently, we conducted chronopotentiometry and 1000 cycles of cycle voltammetry experiments to evaluate the Ce-CPO stability. The extended chronopotentiometry test assesses the exceptional durability of the synthesized Ce-CPO, as evidenced by the little occurrence of potential fluctuations after 10 h of activity (Fig. 7a). In

addition, the inset graph in Fig. 7 demonstrates a little variation in the LSV Curve after 1000 cycles of scanning. To further investigate, following the chronopotentiometry test, structural analyses including FESEM, EDS, and elemental mapping were conducted on the Ce-CPO electrode. In Fig. 7(b, c), micrographs of the Ce-CPO electrode before and after use are shown. As evident in Fig. 7c, after 10 h of electrode usage, the Ce-CPO structure undergoes a reconstruction process. Due to prolonged oxidation, the initial structure transforms into aggregated sheets [54]. Additionally, as shown in the EDS analysis before and after the chronopotentiometry test (Fig. S8(a, b), Electronic Supplementary File), the elements present on the surface of the Ce-CPO structure remained unchanged after the test. This suggests that the elements were well preserved, indicating the suitable stability of the synthesized material. Finally, the elemental mapping analysis before and after electrode usage (Fig. S9(a-l), Electronic Supplementary File) shows that the distribution of elements on the surface did not change significantly during the OER process. The elements remained uniformly dispersed on the surface, as in their initial state, indicating the satisfactory performance of the electrode used.

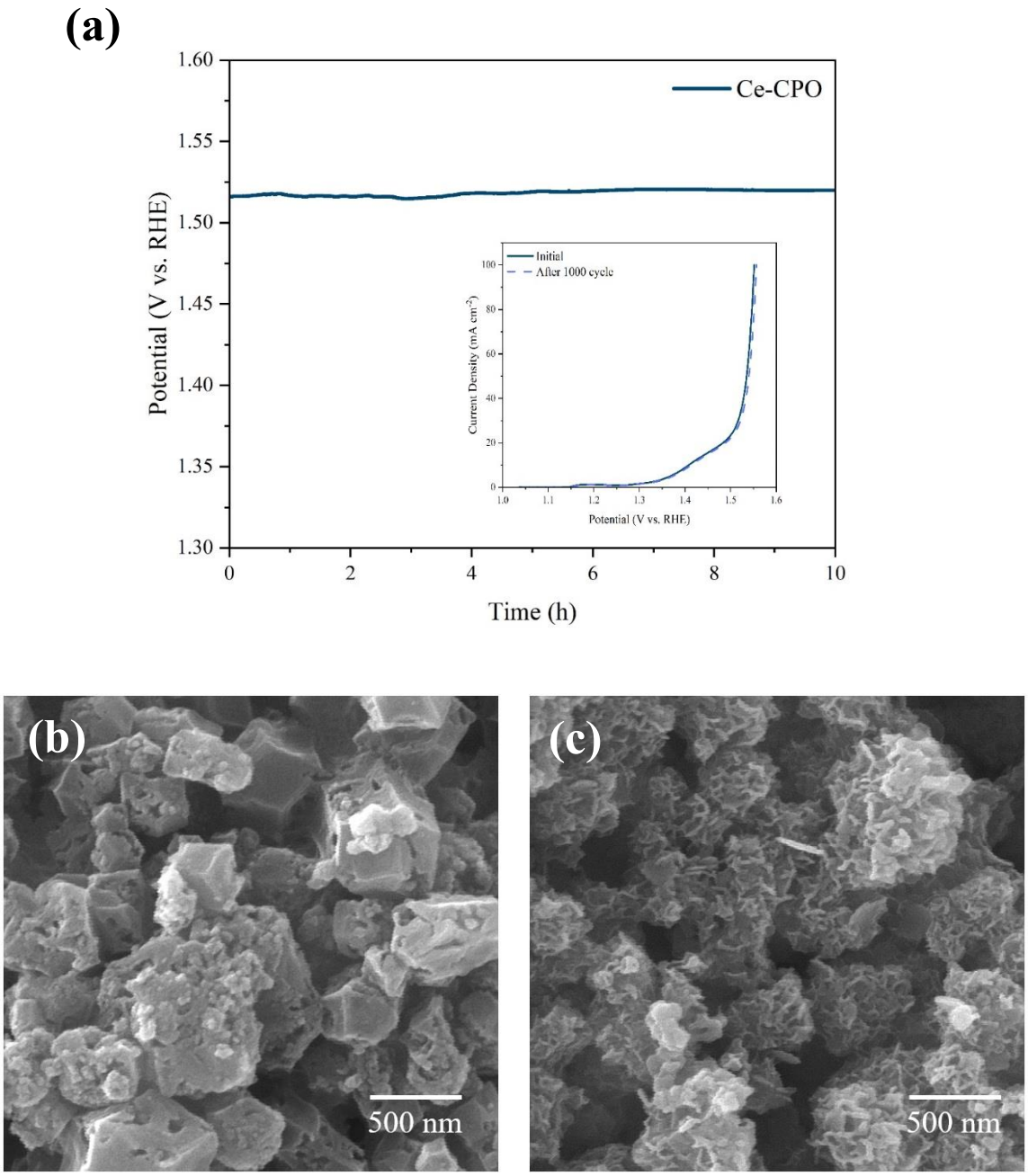


**Fig. 7.** (a) Chronopotentiometry test of Ce-CPO for 10 h (in set is the LSV curves before and after 1000 cycles of CV); FESEM micrographs of Ce-CPO (b) before chronopotentiometry test, (c) after chronopotentiometry test.

Table 1 displays a comparative analysis of the OER efficiency of Ce-CPO in relation to other materials. It is obvious that the performance of the Ce-CPO structure at a current density of 30 mA

363 $cm^{-2}$, which is higher than the current densities reported for other electrodes (10 mA $cm^{-2}$),
364 demonstrates a significantly better performance. This indicates the suitable OER performance of
365 the synthesized amorphous hollow structure. The satisfactory performance of the synthesized
366 electrocatalyst in this process indicates that the improvement in the structure, due to its
367 amorphization and hollowing, enhances electron transfer and increases active sites. Alongside the
368 utilization of the bimetallic structure of ZIF-67, these factors have synergistically contributed to
369 the enhanced performance of the final electrode.

370 **Table 1.** Comparison of the performance of phosphate materials in the OER process.

| Name of electrode | Overpotential (mV)@10 mA $cm^{-2}$ | Reference |
|---|---|---|
| FeCoNi sulfide | 298 | [55] |
| NCP@waste paper-based carbon aerogel | 351 | [56] |
| Ni−Co phosphate | 310 | [57] |
| Ni-doped CoPi | 320 | [58] |
| Hydrous cobalt phosphate thin films | 292 | [59] |
| Ni-Co hydrogen phosphate | 320 | [60] |
| **Ce-CPO** | 286@30 mA $cm^{-2}$ | This work |

371

372 **4. Conclusion**

373 In summary, initially, single-metal and bimetallic ZIF-67 structures with varying amounts of
374 cerium were synthesized using a co-precipitation method. Electrochemical investigations revealed
375 that the (5)CeZIF-67 structure exhibited the lowest overpotential. Subsequently, the (5)CeZIF-67
376 structure was subjected to a phosphatization process under nitrogen gas in a tube furnace, resulting

in the formation of the amorphous and hollow Ce-CPO structure as a novel and highly efficient OER electrocatalyst. In the resultant structure, the presence of active phosphate ions enhanced material activity, hence enhancing electron transport and redox processes. Furthermore, the formation of an amorphous and hollow structure led to significant porosity, providing extensive active surfaces and thereby increasing the surface contact area, which in turn enhanced the rate of electron transfer. Moreover, the superior performance of Ce-CPO compared to CPO demonstrated that the presence of cerium enhanced electron transfer. The bimetallic nature, along with the structural improvements induced by the phosphatization process, played a significant role in improving the overall performance of the final structure. Ultimately, the results obtained from the final structure showed an overpotential of 286 mV at current density of 30 mA $cm^{-2}$ and a Tafel slope of 74.4 mV $decade^{-1}$. Additionally, the resulting structure demonstrated satisfactory stability after a 10 h usage process and even after 1000 cycles.

## References


[1] J. Jean, P.R. Brown, R.L. Jaffe, T. Buonassisi, V. Bulović, Pathways for solar photovoltaics, Energy Environ Sci 8 (2015) 1200–1219. https://doi.org/10.1039/C4EE04073B.

[2] G.J. Gao, J.L. Xu, J. Tang, H.P. Liu, Y.C. Ma, J.M. Luo, Zn constructs micro/nano porous structure to boost efficient oxygen evolution reaction for bulk NiFe alloy, J Alloys Compd 903 (2022) 164004. https://doi.org/10.1016/j.jallcom.2022.164004.

[3] D. Chinnadurai, R. Rajendiran, P. Kandasamy, Bimetallic copper nickel sulfide electrocatalyst by one step chemical bath deposition for efficient and stable overall water splitting applications, J Colloid Interface Sci 606 (2022) 101–112. https://doi.org/10.1016/j.jcis.2021.07.145.

[4] P. Zhang, W. Tan, H. He, Z. Fu, Binder-free quaternary Ni–Fe–W–Mo alloy as a highly efficient electrocatalyst for oxygen evolution reaction, J Alloys Compd 853 (2021) 157265. https://doi.org/10.1016/j.jallcom.2020.157265.

[5] H.S. Jadhav, H.A. Bandal, S. Ramakrishna, H. Kim, Critical Review, Recent Updates on Zeolitic Imidazolate Framework-67 (ZIF-67) and Its Derivatives for Electrochemical Water Splitting, Advanced Materials 34 (2022). https://doi.org/10.1002/adma.202107072.

[6] S. Tan, W. Ouyang, Y. Ji, Q. Hong, Carbon wrapped bimetallic NiCo nanospheres toward excellent HER and OER performance, J Alloys Compd 889 (2021) 161528. https://doi.org/10.1016/j.jallcom.2021.161528.

[7] L. Hong, Z. Liu, X. Zhang, Y. Xue, H. Huang, Q. Jiang, J. Tang, Enhanced OER electrocatalyst performance by sulfur doping trimetallic compounds hybrid catalyst supported on reduced graphene oxide, J Alloys Compd 991 (2024) 174238. https://doi.org/10.1016/j.jallcom.2024.174238.

[8] F. Zeng, C. Mebrahtu, L. Liao, A.K. Beine, R. Palkovits, Stability and deactivation of OER electrocatalysts: A review, Journal of Energy Chemistry 69 (2022) 301–329. https://doi.org/10.1016/j.jechem.2022.01.025.

[9] H. Jiang, J. Gu, X. Zheng, M. Liu, X. Qiu, L. Wang, W. Li, Z. Chen, X. Ji, J. Li, Defect-rich and ultrathin N doped carbon nanosheets as advanced trifunctional metal-free electrocatalysts for the ORR, OER and HER, Energy Environ Sci 12 (2019) 322–333. https://doi.org/10.1039/C8EE03276A.

[10] Y. Wang, R. Zhu, Z. Wang, Y. Huang, Z. Li, Cu induced formation of dendritic CoFeCu ternary alloys on Ni foam for efficient oxygen evolution reaction, J Alloys Compd 880 (2021) 160523. https://doi.org/10.1016/j.jallcom.2021.160523.

[11] A. Saad, Y. Gao, K.A. Owusu, W. Liu, Y. Wu, A. Ramiere, H. Guo, P. Tsiakaras, X. Cai, Ternary $Mo_2NiB_2$ as a Superior Bifunctional Electrocatalyst for Overall Water Splitting, Small 18 (2022). https://doi.org/10.1002/smll.202104303.

[12] L. Chen, J.-T. Ren, Z.-Y. Yuan, Insight into the Active Contribution of N-Coordinated Cobalt Phosphate Nanocrystals Coupled with Carbon Nanotubes for Oxygen Electrochemistry, ACS Sustain Chem Eng 9 (2021) 1856–1866. https://doi.org/10.1021/acssuschemeng.0c08328.

[13] D. Han, L. Hao, R. Wang, Y. Gao, M. Su, Y. Zhang, Design yolk-shelled FeCo layered double hydroxide via a “one-stone-two-birds” strategy for oxygen evolution reaction, Sep Purif Technol 336 (2024) 126363. https://doi.org/10.1016/j.seppur.2024.126363.

[14] H. Cao, P. Qiao, Q. Zhong, R. Qi, Y. Dang, L. Wang, Z. Xu, W. Zhang, In Situ Reconstruction Ni□O Octahedral Active Sites for Promoting Electrocatalytic Oxygen Evolution of Nickel Phosphate, Small 19 (2023). https://doi.org/10.1002/smll.202204864.

[15] J.S. Shaikh, M. Rittiruam, T. Saelee, V. Márquez, N.S. Shaikh, P. Khajondetchairit, S.C. Pathan, M.K. Nazeeruddin, P. Praserthdam, S. Praserthdam, Experimental and first-principles insights into an enhanced performance of Ru-doped copper phosphate electrocatalyst during oxygen evolution reaction, S Afr J Chem Eng 48 (2024) 306–316. https://doi.org/10.1016/j.sajce.2024.03.006.

[16] A.G. Dymerska, B. Środa, B. Zielińska, E. Mijowska, In situ insight into the low-temperature promotion of ZIF-67 in electrocatalytic oxygen evolution reaction, Mater Des 226 (2023) 111637. https://doi.org/10.1016/j.matdes.2023.111637.

[17] J. Wang, C. Chen, N. Cai, M. Wang, H. Li, F. Yu, High topological tri-metal phosphide of CoP@FeNiP toward enhanced activities in oxygen evolution reaction, Nanoscale 13 (2021) 1354–1363. https://doi.org/10.1039/D0NR06615J.

[18] S. Gouadria, M. Abudllah, Z. Ahmad, P. John, M.U. Nisa, S. Manzoor, S. Aman, M.N. Ashiq, M.I. Ghori, Development of bifunctional Mo doped ZnAl2O4 spinel nanorods array directly grown on carbon fiber for supercapacitor and OER application, Ceram Int 49 (2023) 4281–4289. https://doi.org/10.1016/j.ceramint.2022.09.312.

[19] J. Jiang, X. Zhou, H. Lv, H. Yu, Y. Yu, Bimetallic-Based Electrocatalysts for Oxygen Evolution Reaction, Adv Funct Mater 33 (2023). https://doi.org/10.1002/adfm.202212160.

[20] J. Cao, R. Zhao, L. Bai, Y. Wang, Z. Zhang, L. Wu, X. Du, J. Li, Heterogeneous engineering of nickel-iron sulfide with cerium-promoted reconstruction for enhanced oxygen evolution, Appl Surf Sci 627 (2023) 157287. https://doi.org/10.1016/j.apsusc.2023.157287.

[21] W. Gao, F. Ma, C. Wang, D. Wen, Ce dopant significantly promotes the catalytic activity of Ni foam-supported Ni3S2 electrocatalyst for alkaline oxygen evolution reaction, J Power Sources 450 (2020) 227654. https://doi.org/10.1016/j.jpowsour.2019.227654.

[22] J. Feng, S. Ye, H. Xu, Y. Tong, G. Li, Design and Synthesis of FeOOH/$CeO_2$ Heterolayered Nanotube Electrocatalysts for the Oxygen Evolution Reaction, Advanced Materials 28 (2016) 4698–4703. https://doi.org/10.1002/adma.201600054.

[23] F. Esch, S. Fabris, L. Zhou, T. Montini, C. Africh, P. Fornasiero, G. Comelli, R. Rosei, Electron Localization Determines Defect Formation on Ceria Substrates, Science (1979) 309 (2005) 752–755. https://doi.org/10.1126/science.1111568.

[24] J. Bai, C. Chen, Y. Lian, Y. Deng, M. Xiang, Q. Zhou, Y. Tang, Y. Su, Role of amorphous engineering and cerium doping in NiFe oxyhydroxide for electrocatalytic water oxidation, J Colloid Interface Sci 663 (2024) 280–286. https://doi.org/10.1016/j.jcis.2024.02.093.

[25] Q. Liu, F. Kang, T. He, L. Liu, Y. Tang, Fabrication of Ce-doped Hollow $NiCo_2O_4$ Nanoprisms with Heterointerface from MOF-Engaged Strategy for Oxygen Evolution Reaction, Chem Asian J 18 (2023). https://doi.org/10.1002/asia.202300317.

[26] Z. Xue, X. Li, Q. Liu, M. Cai, K. Liu, M. Liu, Z. Ke, X. Liu, G. Li, Interfacial Electronic Structure Modulation of NiTe Nanoarrays with NiS Nanodots Facilitates Electrocatalytic Oxygen Evolution, Advanced Materials 31 (2019). https://doi.org/10.1002/adma.201900430.

[27] D. Ding, K. Shen, X. Chen, H. Chen, J. Chen, T. Fan, R. Wu, Y. Li, Multi-Level Architecture Optimization of MOF-Templated Co-Based Nanoparticles Embedded in Hollow N-Doped Carbon Polyhedra for Efficient OER and ORR, ACS Catal 8 (2018) 7879–7888. https://doi.org/10.1021/acscatal.8b02504.

[28] X. Zhang, G. Li, Y. Zhang, D. Luo, A. Yu, X. Wang, Z. Chen, Amorphizing metal-organic framework towards multifunctional polysulfide barrier for high-performance lithium-sulfur batteries, Nano Energy 86 (2021) 106094. https://doi.org/10.1016/j.nanoen.2021.106094.

[29] W. Zhu, G. Zhu, C. Yao, H. Chen, J. Hu, Y. Zhu, W. Liang, Porous amorphous FeCo alloys as pre-catalysts for promoting the oxygen evolution reaction, J Alloys Compd 828 (2020) 154465. https://doi.org/10.1016/j.jallcom.2020.154465.

[30] J. Han, J. Zhang, T. Wang, Q. Xiong, W. Wang, L. Cao, B. Dong, Zn Doped FeCo Layered Double Hydroxide Nanoneedle Arrays with Partial Amorphous Phase for Efficient Oxygen Evolution Reaction, ACS Sustain Chem Eng 7 (2019) 13105–13114. https://doi.org/10.1021/acssuschemeng.9b02297.

[31] W. Xu, H. Wang, Earth-abundant amorphous catalysts for electrolysis of water, Chinese Journal of Catalysis 38 (2017) 991–1005. https://doi.org/10.1016/S1872-2067(17)62810-9.

[32] M. Gholinejad, Z. Naghshbandi, J.M. Sansano, Zeolitic imidazolate frameworks-67 (ZIF-67) supported PdCu nanoparticles for enhanced catalytic activity in Sonogashira-Hagihara and nitro group reduction under mild conditions, Molecular Catalysis 518 (2022) 112093. https://doi.org/10.1016/j.mcat.2021.112093.

[33] X. Wu, D. Sun, H. Ma, C. Ma, X. Zhang, J. Hao, Activation of peroxymonosulfate by magnetic CuFe2O4@ZIF-67 composite catalyst for the study on the degradation of methylene blue, Colloids Surf A Physicochem Eng Asp 637 (2022) 128278. https://doi.org/10.1016/j.colsurfa.2022.128278.

[34] Z. Panjali, A.A. Asgharinezhad, H. Ebrahimzadeh, S. Karami, M. Loni, M. Rezvani, R. Yarahmadi, S.J. Shahtaheri, Development of a selective sorbent based on a magnetic ion imprinted polymer for the preconcentration and FAAS determination of urinary cadmium, Analytical Methods 7 (2015) 3618–3624. https://doi.org/10.1039/C4AY03066D.

[35] M. Landarani, A.A. Asgharinezhad, H. Ebrahimzadeh, A magnetic ion-imprinted polymer composed of silica-coated magnetic nanoparticles and polymerized 4-vinyl pyridine and 2,6-diaminopyridine for selective extraction and determination of lead ions, New Journal of Chemistry 44 (2020) 7561–7568. https://doi.org/10.1039/D0NJ01109F.

[36] G. Pang, M. Ji, Z. Li, Z. Yang, X. Qiu, Y. Zhao, Electrospinning of ZIF-67 Derived Co-C-N Composite Efficiently Activating Peroxymonosulfate to Degrade Dimethyl Phthalate, Water (Basel) 14 (2022) 2248. https://doi.org/10.3390/w14142248.

[37] N. Heydari, E. Ghorbani-Kalhor, A.A. Asgharinezhad, M. Bahram, M.T. Vardini, Determination of phthalate esters in real matrixes after extraction with a novel magnetic nano-material derived from a metal–organic framework, Microchemical Journal 191 (2023) 108704. https://doi.org/10.1016/j.microc.2023.108704.

[38] T.E. Bakare, M.N. Pillay, W.E. van Zyl, A supercapacitor electrode formed from amorphous Co3(PO4)2 and the normal spinel CoIICoIII2O4, J Solid State Chem 302 (2021) 122422. https://doi.org/10.1016/j.jssc.2021.122422.

[39] C. Sronsri, C. Danvirutai, P. Noisong, Double function method for the confirmation of the reaction mechanism of LiCoPO4 nanoparticle formation, reliable activation energy, and related thermodynamic functions, Reaction Kinetics, Mechanisms and Catalysis 121 (2017) 555–577. https://doi.org/10.1007/s11144-017-1183-1.

[40] J. Yan, Y. Huang, X. Han, X. Gao, P. Liu, Metal organic framework (ZIF-67)-derived hollow CoS2/N-doped carbon nanotube composites for extraordinary electromagnetic wave absorption, Compos B Eng 163 (2019) 67–76. https://doi.org/10.1016/j.compositesb.2018.11.008.

[41] Z. Wang, Z. Wang, J. Wang, H. Shi, C. Wang, Y. Fan, Z. Bai, C. Zhu, X. Yan, Ni, Zn Co-doping ZIF-67-derived electrocatalyst based on CNT film for efficient overall water

splitting, Int J Hydrogen Energy 48 (2023) 29189–29197. https://doi.org/10.1016/j.ijhydene.2023.04.082.

[42] L. Zhao, C. Gong, X. Chen, X. He, H. Chen, X. Du, D. Wang, W. Fang, H. Zhang, W. Li, ZIF-67 derived Mo-CoS2 nanoparticles embedded in hierarchically porous carbon hollow sphere for efficient overall water splitting, Appl Surf Sci 623 (2023) 157030. https://doi.org/10.1016/j.apsusc.2023.157030.

[43] P.K. Katkar, S.J. Marje, S.B. Kale, A.C. Lokhande, C.D. Lokhande, U.M. Patil, Synthesis of hydrous cobalt phosphate electro-catalysts by a facile hydrothermal method for enhanced oxygen evolution reaction: effect of urea variation, CrystEngComm 21 (2019) 884–893. https://doi.org/10.1039/C8CE01653D.

[44] P.K. Katkar, S.J. Marje, S.B. Kale, A.C. Lokhande, C.D. Lokhande, U.M. Patil, Synthesis of hydrous cobalt phosphate electro-catalysts by a facile hydrothermal method for enhanced oxygen evolution reaction: effect of urea variation, CrystEngComm 21 (2019) 884–893. https://doi.org/10.1039/C8CE01653D.

[45] C. Wang, H. Xu, Y. Wang, H. Shang, L. Jin, F. Ren, T. Song, J. Guo, Y. Du, Hollow V-Doped $CoM_x$ (M = P, S, O) Nanoboxes as Efficient OER Electrocatalysts for Overall Water Splitting, Inorg Chem 59 (2020) 11814–11822. https://doi.org/10.1021/acs.inorgchem.0c01832.

[46] A. Shahzad, F. Zulfiqar, M. Arif Nadeem, Cobalt containing bimetallic ZIFs and their derivatives as OER electrocatalysts: A critical review, Coord Chem Rev 477 (2023) 214925. https://doi.org/10.1016/j.ccr.2022.214925.

[47] Z. Song, Y. Wei, Z. Ma, X. Zhang, Y. Mao, J. Luo, X. Zhu, W. Liu, J. Jin, Influence of different sources of cerium on the oxidation-reduction ability and oxygen vacancies of CeO2-MnO in the catalytic oxidation of toluene, Surfaces and Interfaces 24 (2021) 101042. https://doi.org/10.1016/j.surfin.2021.101042.

[48] M. Favaro, J. Yang, S. Nappini, E. Magnano, F.M. Toma, E.J. Crumlin, J. Yano, I.D. Sharp, Understanding the Oxygen Evolution Reaction Mechanism on $CoO_x$ using *Operando*

562 Ambient-Pressure X-ray Photoelectron Spectroscopy, J Am Chem Soc 139 (2017) 8960–
563 8970. https://doi.org/10.1021/jacs.7b03211.

564 [49] P. Bhanja, Y. Kim, B. Paul, J. Lin, S.M. Alshehri, T. Ahamad, Y.V. Kaneti, A. Bhaumik, Y.
565 Yamauchi, Facile Synthesis of Nanoporous Transition Metal-Based Phosphates for Oxygen
566 Evolution Reaction, ChemCatChem 12 (2020) 2091–2096.
567 https://doi.org/10.1002/cctc.201901803.

568 [50] M. Tahir, L. Pan, F. Idrees, X. Zhang, L. Wang, J.-J. Zou, Z.L. Wang, Electrocatalytic
569 oxygen evolution reaction for energy conversion and storage: A comprehensive review,
570 Nano Energy 37 (2017) 136–157. https://doi.org/10.1016/j.nanoen.2017.05.022.

571 [51] X. Yue, W. Ke, M. Xie, X. Shen, Z. Yan, Z. Ji, G. Zhu, K. Xu, H. Zhou, Amorphous
572 CoFe(OH) $_x$ hollow hierarchical structure: an efficient and durable electrocatalyst for
573 oxygen evolution reaction, Catal Sci Technol 10 (2020) 215–221.
574 https://doi.org/10.1039/C9CY02092F.

575 [52] C.C.L. McCrory, S. Jung, J.C. Peters, T.F. Jaramillo, Benchmarking Heterogeneous
576 Electrocatalysts for the Oxygen Evolution Reaction, J Am Chem Soc 135 (2013) 16977–
577 16987. https://doi.org/10.1021/ja407115p.

578 [53] L. Zhao, C. Gong, X. Chen, X. He, H. Chen, X. Du, D. Wang, W. Fang, H. Zhang, W. Li,
579 ZIF-67 derived Mo-CoS2 nanoparticles embedded in hierarchically porous carbon hollow
580 sphere for efficient overall water splitting, Appl Surf Sci 623 (2023) 157030.
581 https://doi.org/10.1016/j.apsusc.2023.157030.

582 [54] Y. Liang, X. Sun, A.M. Asiri, Y. He, Amorphous Ni-B alloy nanoparticle film on Ni foam:
583 rapid alternately dipping deposition for efficient overall water splitting, Nanotechnology 27
584 (2016) 12LT01. https://doi.org/10.1088/0957-4484/27/12/12LT01.

585 [55] Z. Yousefi, A.A. Asgharinezhad, A. Larimi, C. Ghotbi, Highly efficient electrocatalytic
586 water oxidation based on non-precious metal oxides/sulfides derived from a FeCoNi-metal
587 organic framework, J Alloys Compd 1002 (2024) 175214.
588 https://doi.org/10.1016/j.jallcom.2024.175214.

589 [56] C. Cui, X. Lai, R. Guo, E. Ren, W. Qin, L. Liu, M. Zhou, H. Xiao, Waste paper-based carbon
590 aerogel supported ZIF-67 derived hollow NiCo phosphate nanocages for electrocatalytic
591 oxygen evolution reaction, Electrochim Acta 393 (2021) 139076.
592 https://doi.org/10.1016/j.electacta.2021.139076.

593 [57] N.L.W. Septiani, Y.V. Kaneti, K.B. Fathoni, K. Kani, A.E. Allah, B. Yuliarto, Nugraha, H.K.
594 Dipojono, Z.A. Alothman, D. Golberg, Y. Yamauchi, Self-Assembly of Two-Dimensional
595 Bimetallic Nickel–Cobalt Phosphate Nanoplates into One-Dimensional Porous Chainlike
596 Architecture for Efficient Oxygen Evolution Reaction, Chemistry of Materials 32 (2020)
597 7005–7018. https://doi.org/10.1021/acs.chemmater.0c02385.

598 [58] L. Yang, H. Ren, Q. Liang, K.N. Dinh, R. Dangol, Q. Yan, Ultrathin Amorphous Nickel
599 Doped Cobalt Phosphates with Highly Ordered Mesoporous Structures as Efficient
600 Electrocatalyst for Oxygen Evolution Reaction, Small 16 (2020).
601 https://doi.org/10.1002/smll.201906766.

602 [59] P.K. Katkar, S.J. Marje, S.B. Kale, A.C. Lokhande, C.D. Lokhande, U.M. Patil, Synthesis
603 of hydrous cobalt phosphate electro-catalysts by a facile hydrothermal method for enhanced
604 oxygen evolution reaction: effect of urea variation, CrystEngComm 21 (2019) 884–893.
605 https://doi.org/10.1039/C8CE01653D.

606 [60] N.L.W. Septiani, Y.V. Kaneti, K.B. Fathoni, Y. Guo, Y. Ide, B. Yuliarto, X. Jiang, Nugraha,
607 H.K. Dipojono, D. Golberg, Y. Yamauchi, Tailorable nanoarchitecturing of bimetallic
608 nickel–cobalt hydrogen phosphate *via* the self-weaving of nanotubes for efficient oxygen
609 evolution, J Mater Chem A Mater 8 (2020) 3035–3047.
610 https://doi.org/10.1039/C9TA13442E.

611